ADVANCED MATERIALS TECHNOLOGIES
www.advmattechnol.de

Ultrasensitive and Reliable Diamond MEMS Magnetic Force Sensor with 3D Imaging at Room Temperature

*Zilong Zhang, Keyun Gu, Zhijian Zhao, Zheng-Yan Lei, Yi-Hsiu Kao, Meiyong Liao, Takahito Ono, and Masaya Toda**

Developing magnetic force sensors with a simple structure, high sensitivity, and exceptional reliability at room temperature remains challenging due to frequency fluctuations and noise suppression issues. In this work, an ultra-sensitive and highly reliable magnetic force sensor is presented by integrating a single-crystal diamond (SCD) MEMS resonator with a permanent magnetic particle. The magnetic particle serves as the sensing element, enabling precise detection of magnetic field gradients under a field bath. The SCD-based MEMS sensor exhibits outstanding performance, achieving an ultra-low detectable force of 1.8×10^{-16} N/Hz$^{1/2}$, a high magnetic sensitivity of 0.303%/(mT/mm), and a response time of 98.8 ms in the first mode at room temperature. Notably, the resonant frequency fluctuation is remarkably low, reaching 7.89×10^{-4} Hz at room temperature, ensuring stable and reliable operation. Furthermore, a 3D magnetic force imaging sensor based on the SCD platform, capable of visualizing the 3D distribution of magnetic forces is demonstrated. This work lays a solid foundation for the advancement of SCD MEMS-based magnetic imaging sensors, offering unparalleled sensitivity, reliability, and tunable spatial resolution for next-generation magnetic imaging applications.

1. Introduction

Magnetic force sensors play a crucial role in various applications, including precise measurements of magnetic fields, material properties, and forces in sensitive environments. Especially, the weak magnetic force sensors have high sensitivity and accuracy, which makes them essential for advancements in fields such as medical diagnostics, aerospace, and industrial automation.[1–3] Current weak-force magnetic sensors, such as atomic magnetometers, superconducting quantum interference device (SQUID), magnetoresistive sensor, nitrogen-vacancy (NV) sensor, and resonant magnetic force sensors, are widely utilized. Highly sensitive magnetic sensor, known as SQUID, is extensively utilized in detecting biomagnetic signals from human organs. But the SQUID requires cryogenic cooling with complex equipment and is susceptible to electromagnetic interference.[4] Magnetoresistive sensors are compact, highly sensitive, and easily integrated into electronic systems, but they are sensitive to temperature variations and external magnetic disturbances.[5,6] For NV sensors, they can achieve a high sensitivity of aN/Hz$^{1/2}$ level. But they are difficult to control and integrate with other electronics.[7–9] Atomic magnetometers offer exceptional sensitivity in detecting weak magnetic fields but are prone to environmental noises and require careful shielding for optimal performance.[10]

Magnetic resonance force microscopy (MRFM) employs a cantilever-type resonant magnetic force sensor that converts magnetic forces into measurable displacements or frequency changes, offering exceptional spatial resolution and the ability to probe nanoscale structural phenomena. However, it is limited by complex setups, environmental noise, and slow operational speed.[11–13] Typically, the state-of-the-art silicon resonators can achieve force sensitivities of 10^{-16} N/Hz$^{1/2}$ at room temperature and 10^{-18} N/Hz$^{1/2}$ at millikelvin temperatures.[14] In order to achieve high force sensitivity (≈zN/Hz$^{1/2}$), advancements have been made in the development of vertical structure devices at low temperatures, including suspended carbon nanotube oscillators,[2] silicon nanowires,[15] and trapped ion oscillators.[1] These innovations represent significant progress in the field. Magnetic force sensors typically operate at low temperatures, where reduced thermal noise and higher quality (Q) factor significantly improve their performance.[16,17] However, most practical applications require room-temperature operation, where magnetic force sensors offer notable advantages.[18] These include the elimination of uneconomical and complex cryogenic cooling

Z. Zhang, Z. Zhao, Z.-Y. Lei, Y.-H. Kao, T. Ono, M. Toda
Graduate School of Engineering
Tohoku University
6-6-01 Aramaki-Aza-Aoba, Aoba-ku, Sendai, Miyagi 980-8579, Japan
E-mail: toda@tohoku.ac.jp
K. Gu, M. Liao
Research Center for Electronic and Optical Materials
National Institute for Materials Science (NIMS)
1-1 Namiki, Tsukuba, Ibaraki 305-0044, Japan

The ORCID identification number(s) for the author(s) of this article can be found under https://doi.org/10.1002/admt.202500470

DOI: 10.1002/admt.202500470

systems, simpler operation, and compatibility with portable and wearable devices. A promising approach involves resonant magnetic force sensors with mechanical resonators, which convert weak forces into resonance frequency shifts. This design minimizes thermal noise and mechanical drift, ensuring high stability and scalability while enabling precise force measurements at ultra-low levels, even at room temperature. Currently, most resonant magnetic force sensors are fabricated from silicon, which suffers from oxidation and limited reliability under demanding conditions. These limitations highlight the need for more robust materials to improve sensor performance and durability in various applications.

Single-crystal diamond (SCD), a distinctive semiconductor material for micro-electromechanical systems (MEMS) devices, has attracted significant interest due to its remarkable properties, such as excellent thermal conductivity, chemical stability, and biocompatibility. These characteristics make diamond an ideal substrate for resonant magnetic force sensors, enabling high resonant frequency and high Q factor, while improving durability and reliability in dynamic operating conditions.[19,20] Neodymium-Iron-Boron (NdFeB) particles are known for their high magnetic energy density, strong coercivity, excellent remanence, and temperature stability, making them well-suited for high-performance MEMS magnetic sensors that require stable magnetic fields. Additionally, the magnetic field gradient effect, arising from the interaction between a material's magnetic moment and an external magnetic field, is particularly advantageous for high-frequency operations, offering exceptional sensitivity to small magnetic forces.

In this work, we introduce a novel magnetic force imaging sensor that integrates a diamond MEMS resonator with an NdFeB magnetic particle, utilizing the magnetic field gradient effect. The magnetic particle is positioned at the tip of the SCD MEMS resonator. By combining the exceptional properties of SCD MEMS with the strong magnetic interactions of NdFeB particles, the sensor achieves enhanced magnetic force response. The sensor demonstrates outstanding performance, including a low detectable force of 1.80×10^{-16} N/Hz$^{1/2}$, a high magnetic sensitivity of 0.303%/(mT/mm), and a response time of 98.8 ms in the first mode. Additionally, the resonant frequency fluctuation reaches an ultralow value of 7.89×10^{-4} Hz at room temperature. A 3D magnetic force imaging sensor based on the SCD-based platform was also developed to map 3D magnetic force distributions. This work presents a promising approach for designing high-performance MEMS magnetic force sensors with reliable and facile structures, showcasing their potential for applications requiring precise and stable magnetic force measurements.

2. Results and Discussion

2.1. Device Concept and Assembly

The SCD cantilevers were fabricated by a smart-cut method[21] based on the ion-implantation assisted lift-off (IAL) technology[22]. It initiated with the ion-implantation into high temperature and high pressure (HTHP) type-Ib (100) SCD substrate with root mean square (RMS) surface roughness lower than 1 nm. The fabrication process is shown in detail in Figure S1 (Supporting Information). The growth of the SCD epilayer was accomplished by using a microwave plasma chemical vapor deposition (MPCVD) system. The advantages of the epilayer growth are 1) the great enhancement in crystal quality of diamond compared to HTHP diamond, and 2) the accurate control of the thickness of the diamond resonator. The ion-damaged layer was converted to a graphite-like layer during the CVD growth process.

The SCD resonators provide a high-reliability, compact, and advanced platform for fabricating high-performance magnetic sensors. By integrating the SCD cantilever with a NdFeB permanent magnetic particle, we realize a magnetic force sensor with enhanced functionality. NdFeB particles exhibit a unique combination of high magnetic energy density, strong coercivity, excellent remanence, and exceptional temperature stability, making them ideal for high-performance MEMS magnetic force sensors operating in magnetic field gradients. These gradients are particularly suited for high-frequency applications and exhibit high sensitivity to small magnetic forces.

By combining the properties of SCD and NdFeB particles, we leverage their strengths to develop highly sensitive and reliable devices. In this work, we present a magnetic force sensor designed to detect weak magnetic fields, utilizing an SCD resonator coupled with an NdFeB particle, as illustrated in **Figure 1a**. To facilitate heterogeneous integration and lay the foundation for future functional expansion, the fabricated diamond cantilever was transferred to the edge of a Si substrate. A glass needle is utilized to cut the as-fabricated SCD cantilever on the SCD substrate to form the free SCD cantilever. Subsequently, a glass needle controlled by a micromanipulator is used to transfer the free SCD cantilever onto a Si substrate, as shown in Figure 1a. This non-destructive transfer method ensures the precise and stable relocation of the SCD cantilever, which is then secured with a small amount of conductive glue. The NdFeB particle was securely attached to the tip of the SCD cantilever using a small amount of conductive adhesive. The 2D Raman imaging technique enables precise assessment of the quality of the SCD epilayer. The peak position (P_{peak}) was determined by fitting the Raman spectra of each measurement point with a Lorentzian function. The full width at half maximum (FWHM) was obtained by evaluating the dispersion of the Raman spectra using the same Lorentz fitting. The average P_{peak} and FWHM values were derived from the corresponding histograms by applying a Gaussian function fitting. The Raman P_{peak} and FWHM 2D images of a 120 µm-long diamond cantilever are shown in Figure 1b. The histograms for P_{peak} and FWHM are presented in Figure 1c,d, respectively, with the color bars in Figure 1b indicating the value ranges for both P_{peak} and FWHM. While the measured area contains a small region with defective SCD epilayer, the average P_{peak} for the area is 1332.62 cm^{-1}. The crystal quality of the epilayer can be evaluated through the FWHM of the Raman spectra. As shown in Figure 1d, the average FWHM for the measured area is 1.84 cm^{-1}, which is lower than that of the high-pressure and high-temperature (HPHT) substrate before the ion implantation, which is 2.15 cm^{-1} (Figure S2, Supporting Information). The reduced FWHM of the epilayer compared to the original HPHT substrate is attributed to the improved crystalline quality of the epilayer. The HTHP substrate inherently contains defects such as dislocations or strain fields, which broaden the Raman peak. In contrast, the MPCVD growth process yields a high-purity epilayer

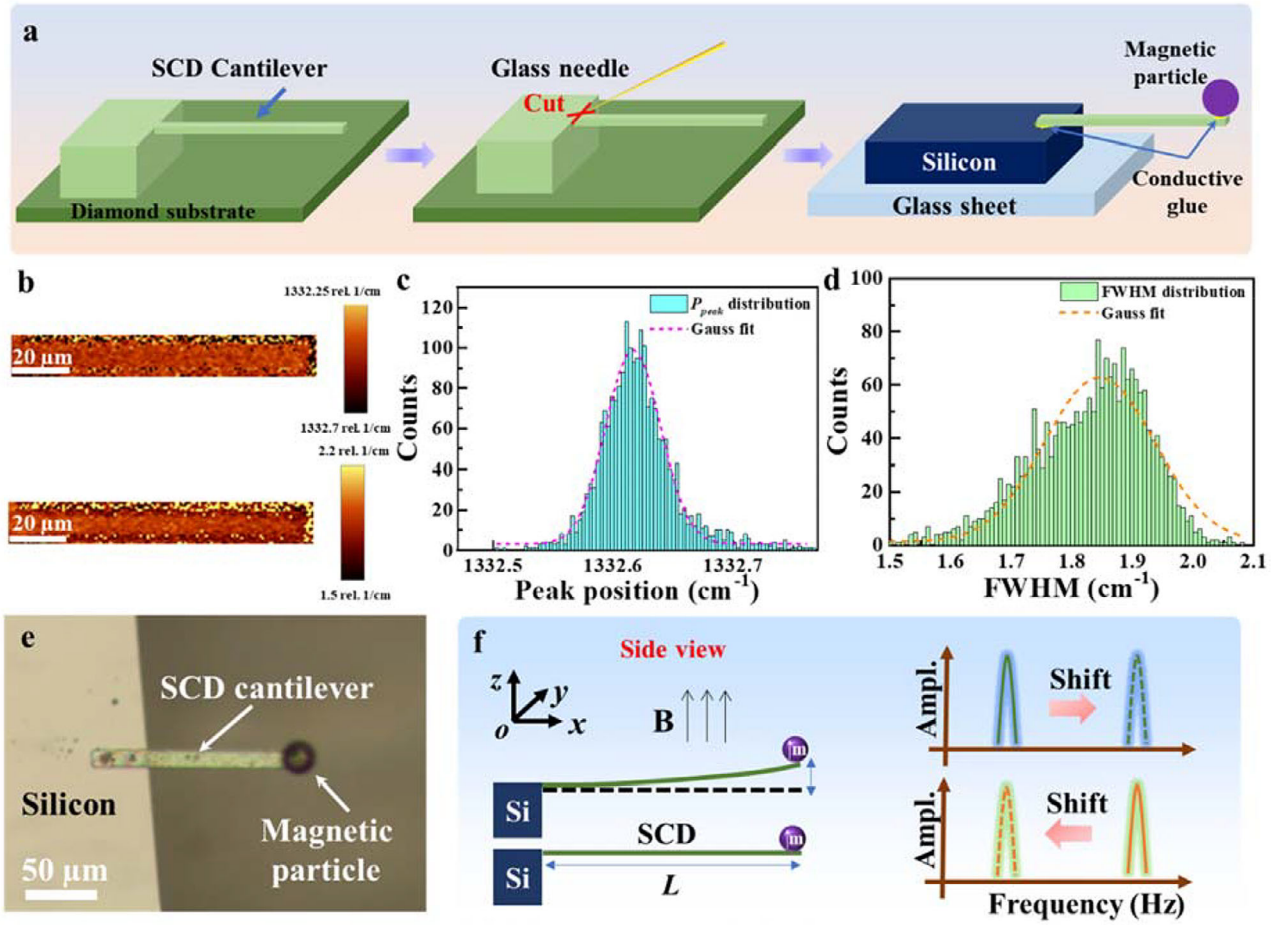

Figure 1. Fabrication process and sensing principle of single-crystal diamond (SCD)-based magnetic force sensor. a) Illustration of the fabrication method of integrating an SCD resonator with a permanent magnetic particle for a magnetic force sensor. The SCD resonator was fixed on the Silicon substrate, and the particle was put on the tip of the SCD resonator via the conductive glue. b) 2D mapping of the Raman P_{peak} and full width half maximum (FWHM) of a 120 μm-length diamond cantilever. c) Histogram distribution of Raman P_{peak}. d) Histogram distribution of FWHM. e) Optical image of a 120 μm length-magnetic force sensor through coupling a SCD cantilever with an NdFeB particle. f) Magnetic force sensing principle of the SCD-based magnetic force sensor. The magnetic force, stemmed from the interaction of the magnetic field gradient and the permanent magnetic particle, is employed for tuning the resonance frequency of this SCD-based sensor. The resonance frequency can shift toward high frequency and low frequency due to the repulsion force and attraction force, respectively.

with lower defect density and reduced internal stress, resulting in a small FWHM. For a one-clamped rectangular micro-resonator without an external force, the resonance frequency mode is given by:[23,24]

$$f = k\frac{t}{L^2}\sqrt{\frac{E}{\rho}} \tag{1}$$

where k takes the values 0.162 and 1.013 for the first and second vibration modes, respectively. E and ρ represent the effective Young's modulus and the effective mass density of the cantilever, respectively, while t and L denote its thickness and length, respectively. Alternatively, the minimum detectable force of the resonator, as limited by thermomechanical noise, can also be expressed as:[14,25]

$$F_{min} = t\sqrt{\frac{w}{lQ}}\sqrt[4]{E\rho}\sqrt{k_B TB} \tag{2}$$

k_B, T, and B represent the Boltzmann constant, temperature, and bandwidth, respectively. The magnetic sensing mechanism relies on the interaction between a magnetic particle affixed to the cantilever tip and an external magnetic field oriented perpendicular to the cantilever's plane, as illustrated in Figure 1e. The as-transferred diamond cantilever has a width of 10 μm and a thickness of 700 nm. The magnetic force exerted on the particle is expressed as follows:[13,26]

$$F = m_z\frac{\partial B}{\partial z} \tag{3}$$

The particle possesses a magnetic moment, m_z, which aligns with an external magnetic field. This magnetic moment, a vector representing the particle's magnetization M, can be calculated by multiplying the magnetization of the particle by its volume V.

The relationship is given by the equation: $m_z = MV$. The magnetic force gradient can be expressed as:

$$F_z' = \frac{dF_z}{dz} = m_z \frac{\partial^2 B}{\partial^2 z} \tag{4}$$

It is noted that the change in the spring constant arises not from a static magnetic force, but from the magnetic force gradient acting on the vibrating NdFeB particle. This gradient, F'_z, directly modifies the effective restoring force experienced by the cantilever during oscillation, thereby altering its effective spring constant, k_{eff}. It is described by the equation:

$$k_{eff} = k + F_z' \tag{5}$$

Consequently, the resonance frequency shift Δf of the NdFeB/SCD sensor, resulting from the magnetic force, is presented as (the detailed derivation is given in Supporting Information):

$$\Delta f = f_B - f_0 \approx -f_0 \frac{F_z'}{2k} \tag{6}$$

f_0 and f_B represent the resonance frequencies of the sensor in the absence and presence of a magnetic field gradient, respectively. Alternatively, the magnetic sensitivity can be defined by the resonance shift in the sensor's response to varying magnetic field gradients, as shown in Figure 1f. The resonance frequency of the sensor can shift toward high frequency and low frequency under the repulsion force and attraction force, respectively. The magnetic sensitivity is characterized by the expressions as follows: $|\Delta f/(f_0 \partial B/\partial z)|$. The $\partial B/\partial z$ indicates the magnetic field gradient. The SCD-based MEMS resonator, utilizing the magnetic field gradient effect, offers a promising system for a high-sensitivity and high-reliability magnetic force sensor.

2.2. Effect of Transfer Method on Vibration Performance

The vibration performance and magnetic sensing were examined through the laser optical system based on the Doppler effect. **Figure 2a** exhibits the measurement setup for the magnetic force sensor. The magnetic field gradients were generated via a coil connected to a DC source. The as-transferred SCD resonator exhibits good vibration performance with a resonance frequency of 172.592 kHz and a Q factor of 3500, as shown in Figure 2b. It is disclosed that the transferred method via the glass needle offers a useful and facile way to transfer the SCD resonator to heterogeneous substrates. In addition, the Q factor is enhanced from 3500 to 6400 through the combination of a magnetic particle on the tip of the SCD cantilever (Figure 2b,c). The increase in Q factor after magnetic particle integration can be attributed to a combination of mechanisms, including the added mass effect and dissipation dilution. The presence of the particle introduces localized strain, which modifies the mode shape and reduces intrinsic energy dissipation, leading to an overall enhancement in Q factor.[27–30] The resonance frequency of the SCD cantilever significantly shifts toward a lower frequency by integrating with a particle. Based on Equation (2), the spring constant and the minimum detectable force (per unit bandwidth) of the magnetic force sensor are 9.0×10^{-3} N m^{-1} and 1.8×10^{-16} N/Hz$^{1/2}$ at room temperature. Figure 2d,e shows the relationship between the resonance spectrum and actuation voltage of the SCD cantilever without and with a magnetic particle, respectively. The peak amplitude of the resonance frequency exhibits a linear dependence on voltage (the insets of Figure 2d,e). Alternatively, the magnetic properties of the NdFeB magnetic particle were examined by the vibrating sample magnetometer (VSM). This magnetic particle was magnetized by a uniform magnetic field before the VSM measurement. The hysteresis loop of the magnetic particle is displayed in Figure 2f. The coercive field H_c and the saturation magnetization M_s of the particle are 1333.1 Oe and 111.9 emu g^{-1}, respectively. This M_s is similar to that of 116 emu g^{-1} of NdFeB particle.[31,32] The higher magnetic energy product $(BH)_{max}$ of this particle can achieve a value that contributes to high magnetic sensing response of the NdFeB/SCD magnetic force sensor

2.3. Magnetic Force Sensing

The SCD MEMS resonator coupled with an NdFeB particle was employed for magnetic sensing through the magnetic field gradient effect. The sensor architecture guarantees both excellent stability and high sensitivity, attributable to 1) the robust, thermal-stable SCD resonator with a temperature coefficient of resonance frequency (TCF) lower than 5 ppm K^{-1}[19,33] and 2) the outstanding magnetic properties of the NdFeB particle. The dependence of relative resonance frequency shift on magnetic field gradient, $|\Delta f/(f_0 \partial B/\partial z)|$, was utilized to indicate the magnetic sensitivity of the SCD-based sensor. In this work, we observed two vibration modes (the first mode and the second mode) of this SCD-based magnetic sensor. The magnetic particle is located at the resonator tip, as shown in Figure 1a, which serves as an antinode for the first vibration mode but not for the second vibration mode. In the first mode, the resonator exhibits a simpler and more uniform motion, resulting in larger vibration amplitudes at the magnetic particle's position. This enhances the coupling between the magnetic particle and the resonator, thereby increasing the sensor's sensitivity to weak magnetic forces. In contrast, in the second mode, the magnetic particle is not positioned at an antinode and therefore experiences smaller vibration amplitudes. The increased stiffness and more complex displacement profile of this mode further limit its sensitivity to small variations in magnetic force. **Figure 3a,b** shows the resonance frequency spectra shift of the 1st mode and 2nd mode of the SCD-based magnetic sensor caused by applying various magnetic field gradients at room temperature, respectively. The amplitudes of the spectra are normalized. Within the positive field gradient range, the frequency shift toward low frequency, showcasing the occurrence of attraction force on the particle. While the frequency moves toward high frequency under negative field gradients, meaning the applied repulsion force on the particle Figure S3 (Supporting Information). Totally, it is elucidated that the resonance frequency shift increases with the magnetic field gradients. The Q factors of these two modes of the SCD-based magnetic sensor exhibit weak change with varying magnetic field gradients (Figure 3c,d).

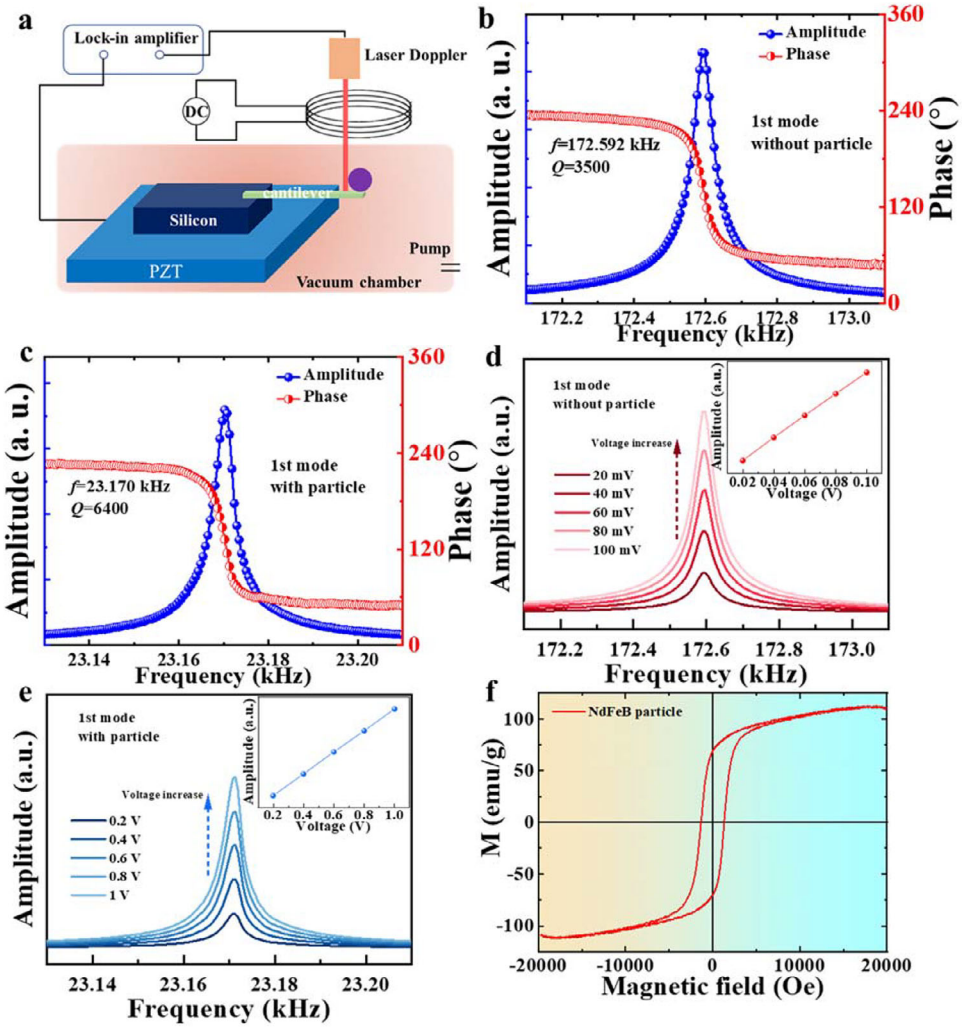

Figure 2. a) Schematic image of measurement setup for vibration and magnetic sensing. b,c) Resonance spectra of the as-transferred SCD resonator without and with a particle, respectively. d,e) Dependences of resonance spectra of the SCD resonator without and with a magnetic particle on the actuation voltage applied to the PZT actuator, respectively. f) In-plane hysteresis loop measured by VSM at room temperature of the permanent magnetic particles.

Through the resonance spectra response to field gradients, the dependences of resonance frequencies of the 1st mode and the 2nd mode of the magnetic force sensor on field gradient are exhibited in **Figure** 4a,b. It can be seen that the resonance frequency shifts linearly increase with magnetic field gradients. The slopes of plots are 70.3 and 231.9 Hz/(mT/mm) for the 1st mode and the 2nd mode, respectively. According to the sensitivity expression, the magnetic sensitivity of the 1st mode is 0.303%/(mT/mm), surpassing the 2nd mode's sensitivity of 0.157%/(mT/mm). This indicates that the magnetic sensitivity of the sensor cannot be effectively enhanced by employing the 2nd mode, which is attributed to the impact of the vibration of the magnetic particle within these two vibration modes on the magnetic sensitivity. Compared to the 2nd mode, the 1st mode exhibits larger displacement amplitudes under the same force and typically benefits from a higher Q factor, leading to lower energy dissipation. These characteristics enhance the sensitivity and reduce the minimum detectable force, making the 1st mode preferable for high-resolution magnetic force detection. In sensing applications, the smallest detectable frequency shift, Δf_{min}, depends on the accuracy of the resonance frequency measurement system. Therefore, identifying and quantifying any noise that affects the frequency stability of the resonator is essential for sensor design.[34] In this work, the Allan deviation is a statistical measure used to quantify the frequency stability of the SCD-based resonant sensor over different averaging times. It is defined as the square root of the Allan variance, which is given by:[34,35]

$$\sigma_A(\tau) = \sqrt{\frac{1}{2(N-1)}\sum_{i=1}^{N-1}\left(\overline{f_{i+1}} - \overline{f_i}\right)^2} \tag{7}$$

where N represents the total number of resonance frequency samples, $f_1, f_2, \ldots, f_N$, each calculated as an average over the integration time τ. The Allan deviation of the 1st mode and the 2nd

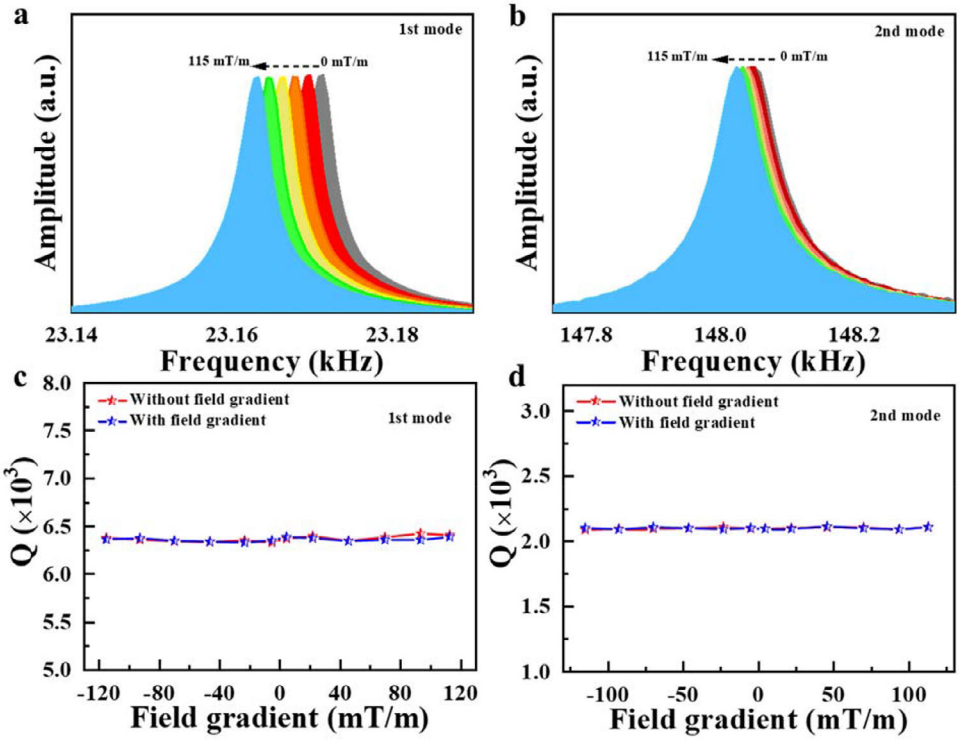

Figure 3. a,b) Resonance spectrum shifts of the 1st mode and 2nd mode of the SCD-based sensor upon positive magnetic field gradients, respectively. c,d) *Q* factor variations of the 1st mode and 2nd mode of the SCD-based sensor without and with applying magnetic field gradients, respectively.

mode of the magnetic force sensor are presented in Figure 4c,d. The analysis reveals that the minimum frequency fluctuations, Δf_{min} of the 1st mode and the 2nd mode are 7.89×10^{-4} and 2.76×10^{-2} Hz, respectively. Using the plot slopes in Figure 4a, the minimum detectable magnetic field gradients are calculated to be 1.12×10^{-5} and 1.19×10^{-4} mT mm^{-1} for the 1st mode and the 2nd mode, respectively. Furthermore, based on Equation (3), the minimum detectable forces at room temperature are determined to be 6.32×10^{-14} and 6.70×10^{-13} N for the 1st mode and the 2nd mode, respectively. For the magnetic force sensor, which consists of an SCD cantilever coupled with a magnetic particle, the 1st mode demonstrates superior performance in achieving a minimal frequency shift and higher force detection sensitivity. **Table 1** displays the sensing performances of representative magnetic force sensors with a resonator-based structure. It is revealed that at room temperature, the present SCD-based magnetic force sensor in our work exhibits excellent force sensitivity and low detection force limitation. Moreover, as indicated by Equation (2), reducing the thickness and achieving a higher *Q* factor in the SCD-based resonator significantly enhances the detection force of the resonator-based sensor. By reducing the thickness of the resonator to below 100 nm while maintaining a *Q* factor of one million, the sensor is expected to reach a magnetic force sensitivity as low as ≈aN/Hz^{1}/^{2}. However, a thinner resonator may experience a decline in *Q* factor due to the surface friction.[14,36] Therefore, careful consideration is required to balance the trade-off between reducing thickness and preserving a high *Q* factor. Alternatively, the response times of the sensor are evaluated by intermittently applying a magnetic field gradient, allowing for an assessment of its performance under dynamic conditions, as shown in Figure 4e,f. The magnetic field gradient was generated using a coil driven by a DC voltage from a signal generator, and was manually switched on and off with a 4-s interval. The sensor exhibits response times of 98.8 ms for the 1st mode and 164.8 ms for the 2nd mode, highlighting the faster response of the 1st mode.

2.4. Magnetic Force Imaging

Magnetic force imaging sensors play a vital role in detecting nanoscale magnetic field distributions with exceptional sensitivity and spatial resolution. They are essential tools for advancing material characterization, biomedical diagnostics, and quantum technology applications.[2,16] Among these, diamond-based sensors stand out for their remarkable durability in extreme environments and their seamless integration with cutting-edge imaging techniques. In this work, a mechanical force technique based on magnetic field gradient is utilized to image the 3D magnetic force distributions. The present magnetic force sensor consists of an SCD MEMS resonator coupled with a permanent magnetic particle (NdFeB). The magnetic fields are generated by a shaped magnet ($3 \times 3 \times 3$ mm^3). The 3D magnetic force imaging was conducted by manually moving the magnet, using a 3D motorized stage with an interval of 1 mm in the *xoy* coordinate plane, as shown in **Figure 5a**. The recorded magnetic response at each position was used to directly generate the 3D map using the visualization software, without additional reconstruction.

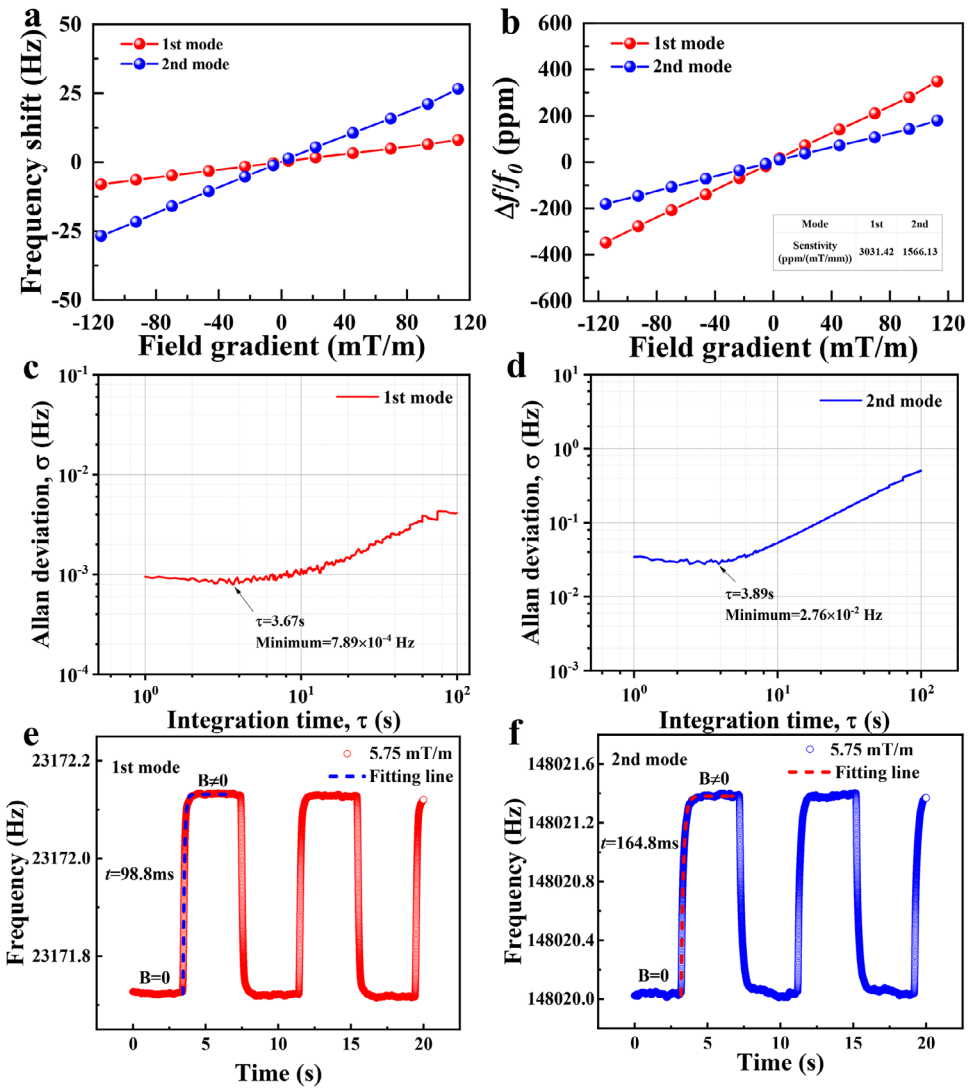

Figure 4. a,b) Dependences of resonance frequency shift of the 1st mode and 2nd mode of the SCD-based sensor upon magnetic field gradients, respectively. The magnetic sensitivity can be expressed in two ways, as indicated by the slopes of the plots. c,d) Allan deviations of the 1st mode and 2nd mode of the SCD-based sensor, respectively. The minimum resonance frequency fluctuation can be obtained at the lowest point of the curves. e,f) Response times of the 1st mode and 2nd mode of the SCD-based sensor to the magnetic field gradient of 5.75 mT m^{-1}.

Each red square represents each movement coordinate position (Figure 5a). Initially, the distance between the magnetic force sensor and the magnet is Z_0 = 10 mm. For the 3D force imaging, this distance changes from Z_0, Z_0 + 1 mm, to Z_0 + 2 mm. Figure 5b,c exhibits the resonance spectra shift with changing x coordinate position as the y = 0 mm and $Z = Z_0$ = 10 mm. The peak amplitude of each resonance spectrum is normalized. It is disclosed that the resonance frequency varies with different x coordinate positions and the Q factor can maintain a week change with the sensor movement. The dependences of the resonance frequency shifts response to magnetic field gradients on the coordinate positions was calculated via the resonance spectra changes. Based on the magnetic sensitivity of 70.24 Hz/(mT/mm) for the 1st mode of the magnetic sensor, the magnetic field gradient, $(dB/dz)_{(x,y)}$ for a specific coordinate position (x, y) is calculated with the known resonance frequency shift, $\Delta f_{(x,y)}$. Through Equation (3), the magnetic force, $F_{(x,y)}$, for this coordinate position is evaluated. Figure 5d–f showcases the magnetic force distributions of a 10 × 10 mm^2 area detected by the SCD-based magnetic force sensor with the Z coordinate varying as Z_0, Z_0 + 1 mm, and Z_0 + 2 mm. The magnetic force decreases with the distance between the sensor and the magnet increasing (Figure 5d–f). It is disclosed that the minimum detectable magnetic force achieves a low value of 5.5 pN at room temperature. The magnetic force sensor made of an SCD resonator with a particle is capable of realizing 3D magnetic force with ≈pN force level, which hosts the promising potential in detecting biological molecules, for example, DNA molecules.[3,41] The spatial resolution and actual detectable force level are constrained by the movement method. Considering the minimum detectable magnetic force for this sensor, it can achieve the fN force level for imaging.

Table 1. Comparison of magnetic force sensing performances of various resonator-based sensors.

Materials	Structure	Principle	f [Hz]	Q	Sensitivity [N/Hz$^{1/2}$]	Limitation [N]	Temperature [°C]	Refs.
Si/NdFeB	NEMS (mirror)	MRFM	5746	4900	1.3×10^{-15}	–	25	[18]
Si/NdFeB	MEMS (cantilever)	MRFM	1640	230	1.1×10^{-13}	–	25	[37]
Si/NdFeB	NEMS (mirror)	MRFM	8000	5000	1.9×10^{-16}	–	25	[38]
Si	NEMS (cantilever)	MRFM	4976	150000	0.82×10^{-18}	–	−273.13 (220 mK)	[39]
Si/Diamond	NEMS (nanowire)	MRFM	7600	130000	2.5×10^{-18}	–	−269.15	[40]
Diamond	NEMS	MRFM	32140	1510000	0.54×10^{-18}	–	−273.14 (100 mK)	[14]
Si/Fe	NEMS (cantilever)	Torque	33977	12000	3.6×10^{-16}	4.6×10^{-13}	25	[26]
Diamond/ NdFeB	MEMS (cantilever)	Field gradient	23170	6400	1.8×10^{-16}	6.3×10^{-14}	25	This work

3. Conclusion

In this work, we developed a highly sensitive and reliable magnetic force sensor by integrating a SCD MEMS resonator with a permanent magnetic particle. The magnetic particle served as a sensing head, enabling the detection of magnetic field gradients. The SCD-based MEMS magnetic transducer demonstrated exceptional performance, achieving a low detectable force of 1.8×10^{-16} N/Hz$^{1/2}$, a high magnetic sensitivity of 0.303%/(mT/mm), and a response time of 98.8 ms in the first mode. Additionally, the resonant frequency fluctuation reaches an ultralow value of 7.89×10^{-4} Hz at room temperature. To extend its capabilities, we developed a 3D magnetic force imaging sensor on the SCD platform, enabling visualization of magnetic force distributions in three dimensions. The magnetic sensing performance can be further enhanced by reducing the thickness of the resonator to less than 100 nm while maintaining a high Q factor. This work establishes a foundation for advanced magnetic imaging sensors based on SCD MEMS resonators integrated with permanent magnetic particles. Owing to its high sensitivity, spatial resolution, and ambient operability, this sensor holds promise for a range of applications such as magnetic resonance imaging (MRI)-inspired sensing, non-invasive biomedical magnetic detection, and localized field mapping in microelectronic and spintronic systems.

4. Experimental Section

Fabrication Process for High Q-Factor Diamond Micro-Cantilevers: In this work, SCD microresonators were fabricated using the smart-cut technique.[19,20] The process began with the growth of a diamond epilayer on HtTHP SCD substrates. Before diamond deposition, the HTHP SCD substrates underwent thorough cleaning, which included boiling in a mixture of acids ($H_2SO_4 + HNO_3$), followed by rinsing with acetone, ethanol, and deionized water. Following cleaning, the carbon ions with an energy of 180 keV and a dose of 10^{16} cm^{-2} were implanted into the substrates. SCD epilayers were then deposited onto these ion-implanted substrates using an MPCVD system. The specific parameters for the MPCVD process were a methane concentration of 0.5%, a hydrogen flow of 500 sccm, a microwave power of 1 kW, a working temperature of 840 °C, and a growth duration of 3 h. During growth, a graphite-like layer ≈200 nm thick formed beneath the diamond surface due to the ion implantation treatment. This layer served as a sacrificial layer to facilitate the release of the resonator structure. Next, a 150 nm-thick aluminum film was deposited onto the SCD epilayer, acting as a metal mask for patterning the epilayer.[24] The patterned SCD was then dry-etched using reactive ion etching (RIE) with an inductively coupled plasma (ICP) system in a pure oxygen environment. To complete the resonator structure, the metal mask was removed by boiling the samples in an acid mixture ($H_2SO_4 + HNO_3$).

After the fabrication process, the SCD sample was annealed at 1100 °C for 3 h under ultrahigh vacuum conditions (<10^{-7} Pa) to reduce defects caused by ion implantation, thus enhancing the Q-factors of the resonators. However, the presence of a non-diamond layer resulting from ion implantation still limited the Q-factor. To address this, oxygen etching was employed to effectively remove defective surface layers, including non-diamond and other imperfections.[42] These surface imperfections had a significant impact on the resonator's performance. Following this treatment, the resonators were annealed again at 650 °C for 10 h in an oxygen environment to further improve Q-factors.

A Smart Method for Transferring a Free Resonator or a Particle on Hetero-Substrates: The magnetic force sensor was configured by coupling an SCD MEMS resonator with an NdFeB particle, as illustrated in Figure 1a. The free SCD cantilever stems from the as-fabricated SCD cantilever on the SCD substrate, which was cut by a glass needle. Then, through an optical microscope, a glass needle controlled by a micromanipulator was utilized to pick up the free SCD cantilever from the Si substrate. The SCD cantilever was precisely and stably transferred via this non-destructive transfer method, and fixed with a small amount of conductive glue. The sample was heated up to 180 °C to fix the SCD cantilever on the Si substrate. After the above process, a 14 µm-diameter NdFeB magnetic particle was also picked up and placed on the tip of the SCD cantilever using a glass needle. The transferred method is similar to that of the free SCD cantilever. Prior to the vibrating sample magnetometer (VSM) measurement, the NdFeB particle was in an annealed state and magnetized using a 694 mT magnetic field. The magnetic moment, which is a vector quantity of the magnetization m of the magnetic particle, can be calculated from the magnetization M of the particle and the volume of the magnetic particle V, using the following equation of $m = MV$.

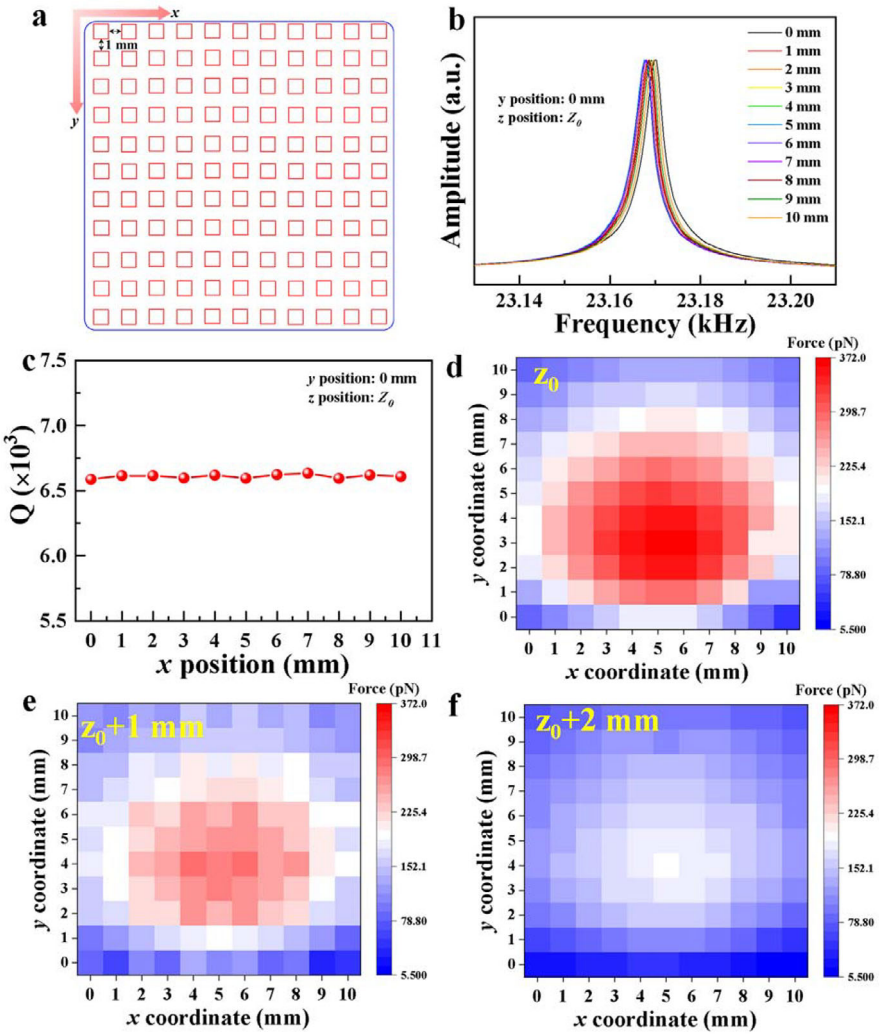

Figure 5. a) Schematic image of movement steps along the *x* coordinate and the *y* coordinate with a 1 mm interval in the *xoy* plane for magnetic force sensing. b,c) Dependences of the resonance spectrum and *Q* factor of the magnetic force sensor on the *x* position as the *y* position is fixed at 0 mm, respectively. The distance between the sensor and the magnet is $Z_0 = 10$ mm. d–f) Magnetic force imaging of the magnetic force sensor with changing of *Z* coordinate as Z_0, $Z_0 + 1$ mm, and $Z_0 + 2$ mm.

Materials Characterization and Readout of Resonance Signals: The hysteresis loop of the permanent magnetic particle was measured using a VSM (TM-VSM5050-SMS, Japan). The system was equipped with a 1800 lines/mm monochromator grating and a cooled charge-coupled device detector. To assess the out-of-plane resonance performance of the SCD cantilever, both with and without a magnetic particle, an optical setup based on the Doppler effect was employed, as illustrated in Figure 2a. This setup used a focused He–Ne laser (633 nm, <1 mW) directed vertically onto the substrate. A lock-in amplifier (HF2LI from Zurich Instruments) was used to capture the resonance signal. All experiments were conducted in a vacuum chamber with a pressure below 10^{-2} Pa. The resonators were driven by a lead zirconate titanate (PZT) actuator. For magnetic sensing measurements, magnetic field gradients were applied using a coil connected to a DC power source.

Supporting Information

Supporting Information is available from the Wiley Online Library or from the author.

Acknowledgements

The authors greatly thanked Dr. Meiyong Liao (NIMS) for his help in offering the diamond MEMS cantilevers. This work was partially supported by a Grant-in-Aid of JSPS KAKENHI (Grant Nos. 24K00828 and 24H00287).

Conflict of Interest

The authors declare no conflict of interest.

Data Availability Statement

All data needed to evaluate the conclusions in the paper are present in the paper and/or the Supplementary Information. Other relevant data of this study are available from the corresponding author upon reasonable request.

Keywords

3D imaging, magnetic force sensor, resonator, single-crystal diamond

Received: March 5, 2025
Revised: April 30, 2025
Published online:

[1] M. J. Biercuk, H. Uys, J. W. Britton, A. P. VanDevender, J. J. Bollinger, *Nat. Nanotechnol.* **2010**, *5*, 646.
[2] J. Moser, J. Güttinger, A. Eichler, M. J. Esplandiu, D. Liu, M. Dykman, A. Bachtold, *Nat. Nanotechnol.* **2013**, *8*, 493.
[3] T. Liu, T. Cai, J. Huo, H. Liu, A. Li, M. Yin, Y. Mei, Y. Zhou, S. Fan, Y. Lu, *Nucleic Acids Res.* **2024**, *52*, 86.
[4] H. Weinstock,*in SQUID Sensors: Fundamentals, Fabrication and Applications*, Springer Science + Business Media, Berlin, Germany **2012**.
[5] S. Yang, J. Zhang, *Chemosensors* **2021**, *9*, 211.
[6] L. Jogschies, D. Klaas, R. Kruppe, J. Rittinger, P. Taptimthong, A. Wienecke, L. Rissing, M. C. Wurz, *Sensors* **2015**, *15*, 28665.
[7] F. Casola, T. Van Der Sar, A. Yacoby, *Nat. Rev. Mater.* **2018**, *3*, 1.
[8] J. L. Webb, L. Troise, N. W. Hansen, J. Achard, O. Brinza, R. Staacke, M. Kieschnick, J. Meijer, J.-F. Perrier, K. Berg-Sørensen, *Front. Phys.* **2020**, *8*, 522536.
[9] K. Yamakawa, Y. Ochiai, T. Ono, M. Toda, *Functional Diamond* **2024**, *4*, 2389801.
[10] X. Bai, K. Wen, D. Peng, S. Liu, L. Luo, *Front. Phys.* **2023**, *11*, 1212368.
[11] D. Rugar, R. Budakian, H. Mamin, B. Chui, *Nature* **2004**, *430*, 329.
[12] M. R. Koblischka, U. Hartmann, *Ultramicroscopy* **2003**, *97*, 103.
[13] M. Toda, T. Ono, *J. Magn. Reson.* **2021**, *330*, 107045.
[14] Y. Tao, J. M. Boss, B. Moores, C. L. Degen, *Nat. Commun.* **2014**, *5*, 3638.
[15] J. M. Nichol, E. R. Hemesath, L. J. Lauhon, R. Budakian, *Appl. Phys. Lett.* **2008**, *93*, 193110.
[16] M. Poggio, C. L. Degen, *Nanotechnology* **2010**, *21*, 342001.
[17] O. Kazakova, R. Puttock, C. Barton, H. Corte-León, M. Jaafar, V. Neu, A. Asenjo, *J. Appl. Phys.* **2019**, *125*, 060901.
[18] M. Toda, G. Xue, T. Ono, *IEEJ Trans. Sens. Micromach.* **2022**, *142*, 224.
[19] Z. Zhang, H. Wu, L. Sang, Y. Takahashi, J. Huang, L. Wang, M. Toda, I. M. Akita, Y. Koide, S. Koizumi, *ACS Appl. Mater. Interfaces* **2020**, *12*, 23155.
[20] Z. Zhang, H. Wu, L. Sang, J. Huang, Y. Takahashi, L. Wang, M. Imura, S. Koizumi, Y. Koide, M. Liao, *Carbon* **2019**, *152*, 788.
[21] M. Liao, S. Hishita, E. Watanabe, S. Koizumi, Y. Koide, *Adv. Mater.* **2010**, *22*, 5393.
[22] P. Olivero, S. Rubanov, P. Reichart, B. C. Gibson, S. T. Huntington, J. Rabeau, A. D. Greentree, J. Salzman, D. Moore, D. N. Jamieson, *Adv. Mater.* **2005**, *17*, 2427.
[23] W. Weaver Jr, S. P. Timoshenko, D. H. Young, in *Vibration Problems in Engineering*, John Wiley & Sons, Hoboken, NJ, USA **1991**.
[24] M. Liao, *Functional Diamond* **2022**, *1*, 29.
[25] S. Castelletto, L. Rosa, J. Blackledge, M. Z. Al Abri, A. Boretti, *Microsyst. Nanoeng.* **2017**, *3*, 1.
[26] T. Ono, M. Esashi, *Rev. Sci. Instrum.* **2003**, *74*, 5141.
[27] A. H. Ghadimi, S. A. Fedorov, N. J. Engelsen, M. J. Bereyhi, R. Schilling, D. J. Wilson, T. J. Kippenberg, *Science* **2018**, *360*, 764.
[28] L. Sang, M. Liao, X. Yang, H. Sun, J. Zhang, M. Sumiya, B. Shen, *Sci. Technol. Adv. Mater.* **2020**, *21*, 515.
[29] A. Beccari, D. A. Visani, S. A. Fedorov, M. J. Bereyhi, V. Boureau, N. J. Engelsen, T. J. Kippenberg, *Nat. Phys.* **2022**, *18*, 436.
[30] R. Shaniv, S. K. Keshava, C. Reetz, C. A. Regal, *Phys. Rev. Appl.* **2023**, *19*, L031006.
[31] R. Kuchi, V. Galkin, S. Kim, J.-R. Jeong, S.-j. Hong, D. Kim, *IEEE Magn. Lett.* **2022**, *13*, 1.
[32] V. Galkin, R. Kuchi, S.-J. Kwon, T.-h. Kim, J.-g. Lee, J.-R. Jeong, D. Kim, *J. Magn.* **2024**, *29*, 1.
[33] Z. Zhang, Y. Wu, L. Sang, H. Wu, J. Huang, L. Wang, Y. Takahashi, R. Li, S. Koizumi, M. Toda, *Mater. Res. Lett.* **2020**, *8*, 180.
[34] M. Sansa, E. Sage, E. C. Bullard, M. Gély, T. Alava, E. Colinet, A. K. Naik, L. G. Villanueva, L. Duraffourg, M. L. Roukes, *Nat. Nanotechnol.* **2016**, *11*, 552.
[35] P. Sadeghi, A. Demir, L. G. Villanueva, H. Kähler, S. Schmid, *Phys. Rev. B* **2020**, *102*, 214106.
[36] K. Y. Yasumura, T. D. Stowe, E. M. Chow, T. Pfafman, T. W. Kenny, B. C. Stipe, D. Rugar, *J. Microelectromech. Syst.* **2000**, *9*, 117.
[37] G. Xue, M. Toda, X. Li, X. Wang, T. Ono, *IEEE Sens. J.* **2021**, *21*, 22578.
[38] Y.-J. Seo, M. Toda, Y. Kawai, T. Ono, *IEEJ Trans. Sens. Micromach.* **2014**, *134*, 166.
[39] H. Mamin, D. Rugar, *Appl. Phys. Lett.* **2001**, *79*, 3358.
[40] Y. Tao, C. L. Degen, *Nano Lett.* **2015**, *15*, 7893.
[41] M. Rief, F. Oesterhelt, B. Heymann, H. E. Gaub, *Science* **1997**, *275*, 1295.
[42] Z. Zhang, G. Chen, K. Gu, S. Koizumi, M. Liao, *Functional Diamond* **2023**, *3*, 2221280.